

# High and low cycle fatigue performance comparison between micro-alloyed and TMT rebar



Surajit Kumar Paul<sup>a,\*</sup>, Pritam Kumar Rana<sup>b</sup>, Debdulal Das<sup>b</sup>, Sanjay Chandra<sup>a</sup>, Saurabh Kundu<sup>a</sup>

<sup>a</sup> R&D, Tata Steel Limited, Jamshedpur 831007, India

<sup>b</sup> Department of Metallurgy and Materials Engineering, Bengal Engineering and Science University, Shibpur 711103, India

## HIGHLIGHTS

- MA rebar has better high and low cycle fatigue behavior than that of TMT rebar.
- Fatigue crack initiates from the transverse rib root and propagate along the same region.
- Stress concentration and high stress triaxiality observed at the root of the transverse rib.

## ARTICLE INFO

### Article history:

Received 25 October 2013

Received in revised form 17 December 2013

Accepted 19 December 2013

### Keywords:

TMT rebar  
Micro-alloyed rebar  
High cycle fatigue  
Low cycle fatigue  
Seismic resistance  
Stress concentration  
Stress triaxiality  
Transverse rib

## ABSTRACT

High and low cycle fatigue performance of micro-alloyed and TMT rebars are compared through experimental investigation. Micro-alloyed rebar shows better fatigue performance than TMT rebar. It is experimentally observed in both micro-alloyed and TMT rebars that for high and low cycle fatigue, crack initiates from the transverse rib root and propagate along the same region. From finite element simulation, it is noticed that the stress concentration takes place at the root of the transverse rib and stress triaxiality becomes higher in the same region. At the transverse rib root, tensile strain accumulation is noticed in simulation. The experimental observation is explained with the help of simulation result that fatigue crack initiate and propagate along the transverse rib root.

© 2013 Elsevier Ltd. All rights reserved.

## 1. Introduction

Reinforced concrete (RC) structures are widely used in civil engineering works and rebars represent the basic strengthening element of RC structures. Rebars are responsible for carrying, distributing and controlling loads and displacements. In recent times global trend in the construction industry is observed towards weight reduction by using of high strength, superior ductility and weldable steel. The use of high strength rebars in concrete structures can greatly minimize the consumption of reinforcing steel up to a certain extent or improve the strength of reinforced structures [1]. In the past, technologies for achieving high strength in steel bars involved either alloying of steel (mainly by carbon addition) or work hardening through cold twisting operations. Reinforcement bars that attain high strength through alloying are

generally used in the as rolled condition. These rebars, which are usually of high carbon content (~0.3–0.5 wt.%), possess restricted weldability, since preheating that is necessary and low-heat-input during welding. On the other hand, work-hardened rebars, which have a lower carbon content (0.06–0.15 wt.%) and about 1 wt.% Mn, has better weldability than alloyed as-rolled rebars. Work-hardened rebars, however, tend to lose their strength upon exposure to temperatures higher than 300 °C a situation which might often arise during welding or hot bending operations at the construction site [2].

In recent times, thermo mechanical treatment (TMT) has emerged as a technically attractive route for producing high strength rebars of lean steel chemistry [3]. TMT rebars has a unique composite microstructure: a ductile ferrite-pearlite core and a tough tempered martensite rim. This composite microstructure is primarily responsible for the combination of contradictory metallurgical properties of high strength and ductility. However welding of TMT rebar consequences alteration of martensite structure and as a result strength reduces. The TMT rebars are produced by three

\* Corresponding author. Tel.: +91 657 2148919/13; fax: +91 657 2271748.

E-mail addresses: [paulsurajit@yahoo.co.in](mailto:paulsurajit@yahoo.co.in), [surajit.paul@tatasteel.com](mailto:surajit.paul@tatasteel.com) (S.K. Paul).

stage processes: hot rolling of rebar, quenching through high pressure water jets which result in the formation of a rim of martensite on the surface, and in last stage the surface layer is tempered due to the flow of heat from the core of the bar to the surface, i.e. the martensitic rim gets self tempered [4]. Precise control of quenching process required to control martensite rim thickness and hence uniform mechanical properties throughout the TMT rebar's length. On the contrary, micro-alloyed (MA) rebar (lower carbon content and strengthening by fine carbides or carbo-nitrides) is produced by two stage processes: hot rolling of rebar and air cooling. For MA rebar, the microstructure throughout the cross section is uniform and simple production process consequences uniform mechanical properties throughout the length of MA rebar. The most prominent advantage of MA rebar over the TMT rebar lies in the ductility. The higher ultimate tensile strength to yield stress ratio in the MA rebar offers better fatigue resistance than the conventional TMT rebar. However, the addition of micro-alloying elements may result higher production cost and require controlled welding. The TMT and MA rebars have own advantages and disadvantages, those are the outside scope of the present work. In the present work, fatigue properties of TMT and MA rebars are investigated, which have two different microstructures: TMT rebar has a tough tempered martensite rim on the outer surface and a ductile ferrite–pearlite core, whereas MA rebar has uniform ferrite–pearlite microstructure.

The majority of the civil engineering structures use TMT rebar with minimum yield stress of 500 MPa as reinforcement in household and large structures like stadiums, bridges etc. Earthquakes cause loading on the reinforcing steel in the region of low cycle fatigue. Sheng and Gong [5] investigated seismic ruins of Tangshan (China) and confirmed that the failure model of building structural steels under earthquake loading is low cycle fatigue (LCF). Considering the importance of LCF to assess seismic response, many researchers investigated LCF properties of rebars [6–11] and structural steels [12,13]. A reinforcement–concrete building is a composite structure of concrete and rebar from the perspective of material science. The brittle materials like concrete and brick masonry are the main body of the building supports which can only withstand pressure. At the time of an earthquake the rebar–concrete structure withstands the high-strain alternating load. The rebars inside the structure bear all tensile load, just like a skeleton maintaining the integrity of the structure. As long as the rebar does not fail, there will be no catastrophic collapse of buildings and people inside will set chance to escape for survival. Entire north and north-east India is earthquake prone regions. Therefore, building of seismic resistant housing and infrastructure are necessary in country like India. Thus to assess seismic resistant property the LCF investigation is justified.

On the other hand, parts of road networks, bridges and offshore structures are subjected to cyclic loading due to their operational loads and therefore it is mandatory to evaluate high cycle fatigue (HCF) property of rebar before use their. For example during the operational lives of 30 years, the offshore structures are subjected to more than  $10^7$  cycles of stress reversal caused by the action of waves. The traffic induced stress reversal on a highway bridges on 50 years life span may raise up to  $3 \times 10^8$  cycles [14,15]. All those stress reversal are small in nature and large in number of cycles, as a consequence HCF is prominent in those applications. In the developing country like India massive infrastructure projects are building up and to ensure their design life span, HCF investigation is justified.

For the present investigation, TMT and MA rebars are selected. Both TMT and MA rebars have almost same yield strength 500 MPa, same diameter 8 mm and rib profile. However, TMT has composite microstructure (a tough tempered martensite rim on the outer surface and a ductile ferrite–pearlite core) and MA has

uniform microstructure (ferrite–pearlite). The HCF and LCF behavior of TMT and MA rebars are compared in the current work.

## 2. Experimental procedure

The tensile, HCF and LCF experiments are conducted on 500 steel grade TMT and MA steel rebars. Diameter and rib profiles of MA and TMT rebars are exactly same. Therefore nominal cross-sectional area-based quality index  $Q_b$  as mentioned by Apostolopoulos and Passialis [16] is exactly same for MA and TMT rebars. The materials are delivered in the form of ribbed bars of nominal diameter of 8 mm. The chemical compositions of the TMT rebar are 0.2 wt.% C, 0.97 wt.% Mn, 0.16 wt.% Si and 0.16 wt.% Cr; and MA rebar are 0.1–0.2 wt.% C, 0.5–1.5 wt.% Mn, 0.1–0.6 wt.% Si and 0–0.1 wt.% V.

From the rebars, tensile specimens of 300 mm length (200 mm gauge length) are cut. Tensile tests are conducted for TMT and MA rebars in a 100 kN servo-hydraulic dynamic testing machine (INSTRON made) with constant strain rate of 0.001/S. Strain during tensile test is measured by a video extensometer. Test setup for tensile and fatigue testing is shown in Fig. 1. Tensile properties of TMT and MA rebars are tabulated in Table 1. From the same rebars, specimens of length 300 mm (200 mm gauge length) are also cut for the HCF tests according to the specification BS 4449 [17]. HCF tests are conducted for TMT and MA rebars in a same 100 kN servo-hydraulic testing machine with test frequency of 30 Hz. In all HCF experiments, stress ratio (ratio of minimum and maximum stress during cycling) of 0.2 is maintained as per the BS 4449 specification [17].

Specimens of length 125 mm (25 mm gauge length) are also cut for the LCF tests. Currently, there is no specification by which LCF tests on reinforcing steel bars can be performed. Current specifications for LCF tests (such as [18]) require proper forming of the specimen either to a uniform gauge section or to an hourglass section. However, such forming will alter the ribbed nature of reinforcing bars leading to misleading test results. To avoid this, the tests are conducted on the rebar specimens in as received surface condition. With this gauge length no buckling is observed thus no anti-buckling device is required. In all LCF experiments, strain rate of 0.001/S is maintained and tests frequencies are altered accordingly. In the same servo-hydraulic dynamic testing machine LCF tests are also conducted and load–strain data are stored through an automatic data login system.

## 3. Result and discussion

### 3.1. Characterization of as received material

Transverse sections of the TMT and MA rebars are polished and etched with 2% nital to observe the general macrostructure. A dark peripheral rim of tempered martensite and a gray core corresponding to the ferrite–pearlite interior is observed in the TMT specimen (Fig. 2a), whereas for MA specimen throughout the cross section

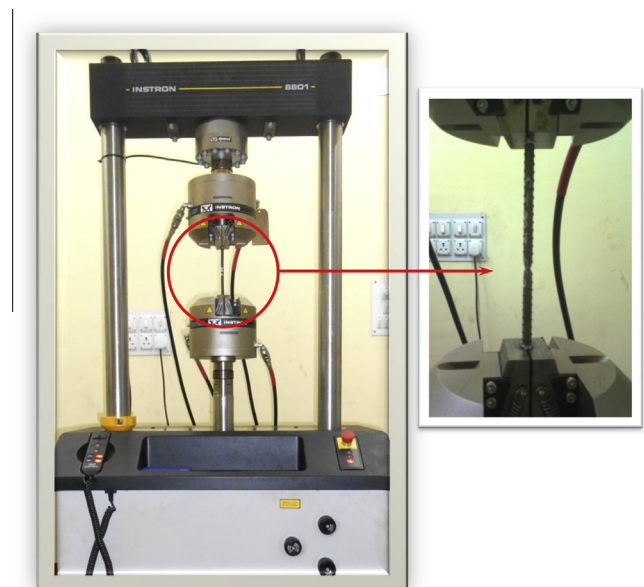
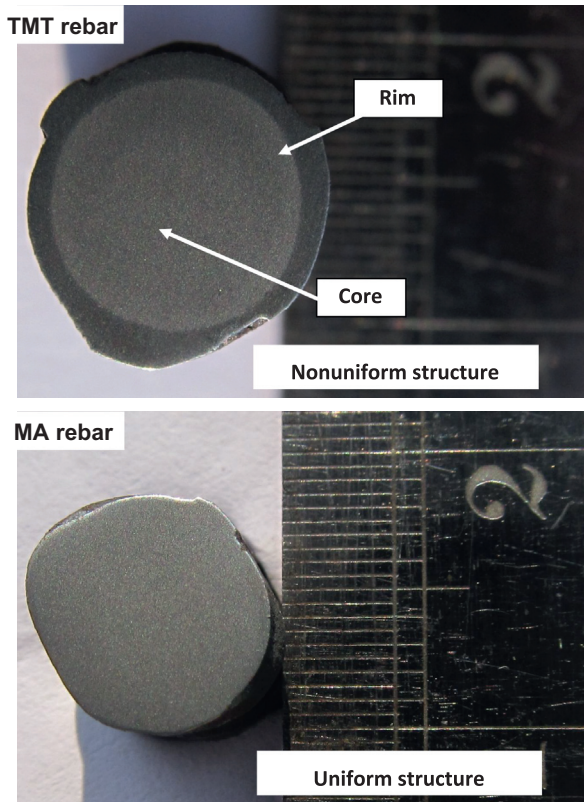


Fig. 1. Tensile and fatigue testig setup: figure showing tensile testing.

**Table 1**  
Tensile properties of TMT and MA rebars.

Material	Yield stress, MPa	Ultimate tensile stress, MPa	Uniform elongation, %
TMT rebar	551	649	12.7
MA rebar	502	705	14.8



**Fig. 2.** Macroscopic view of TMT and MA rebars.

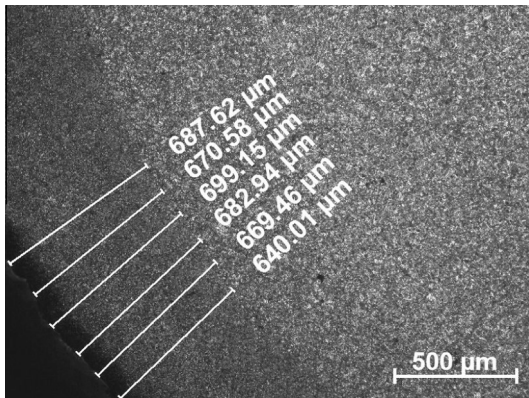


**Fig. 3.** Martensite rim thickness in TMT rebar of 8 mm diameter.

uniform microstructure ferrite–pearlite interior is observed (Fig. 2b). The tempered martensite rim is concentric, indicating uniform quenching of the bar surface in the cooling zone. This uniform rim of tempered martensite results in consistent mechanical properties along the length of the bar. The width of tempered martensite rim for TMT rebar is depicted in Fig. 3.

Optical microscopic examinations are carried out on nital-etched transverse sections of 8 mm diameter TMT and MA rebars. Optical microstructure of rim region and core region of TMT rebar are shown in Fig. 4(a) and (b). The TMT rebar essentially exhibited a composite microstructure comprising a ferrite–pearlitic core and a tempered martensite rim. Similarly for MA rebar, the Optical microstructure of rim region and core region are shown in Fig. 4(c) and (d). The MA rebar actually exhibits a uniform ferrite–pearlitic microstructure throughout its cross section. To confirm the fact the Vickers micro-hardness test is carried out for MA and TMT rebars. Vickers micro-hardness of MA and TMT rebars is depicted in Fig. 5, the distance of profiles are considered from the edge to center of the rebars. Fig. 5 shows almost uniform hardness for MA rebar, whereas higher hardness in the rim region and lower hardness in the center for TMT rebar.

### 3.2. Tensile fracture surfaces

The main observations on tensile fracture surfaces are that both TMT and MA rebars showed microvoid coalescence-type ductile fracture with small voids slightly more evident in the former (Fig. 6). In general during tensile loading of any specimen, crack initiation occurs at the center by fracturing the inclusion/matrix interfaces or from preexisting microcracks at the interface (e.g., MnS inclusion [19]/matrix interface) of the grain boundaries, and/or within the grains. The microcrack produces a triaxial stress state in the specimen, which promotes void nucleation and growth around the larger particles. Further strain causes these voids to coalesce. At some point, the deformation and longitudinal crack growth cannot continue when the work hardening capacity is exhausted and final failure takes place.

The tensile fracture surfaces at room temperature are composed of microvoid coalescence-type fractures. Since core of the MA rebar has coarser ferrite grain sizes, the spacing between pearlite colonies is arguably higher (Fig. 4d). As a result, an individual microvoid needs to grow to a greater extent to join with adjacent voids. This overall process makes the ductile voids in core of the MA rebar seem somewhat coarser, which can be distinguished under close observation. In the contrary, the spacing between pearlite colonies is small (Fig. 4b), as a consequence the ferrite grain size for the core of the TMT rebar is also small. Therefore, microvoid initiation sites are more and an individual microvoid needs to grow to a lesser extent to join with adjacent voids. Thus, the ductile voids in core of the TMT rebar are refined, distinguished in Fig. 6(a).

### 3.3. High cycle fatigue performance

Comparison of HCF performance between MA and TMT rebars are shown in Fig. 7. The stress range (stress ratio 0.2) versus number of cycle to failure is plotted for MA and TMT rebars. It can be observed from Fig. 7 that at higher stress level the stress range versus number of cycle to failure curve for TMT and MA rebar almost close to each other while spread out with decreasing stress level. That means HCF strength (No. of cycles to failure in other words) is close for both types of rebars (TMT and MA) at high stress ranges and at lower stress ranges the high cycle fatigue strength of MA rebar is significantly higher than TMT rebar. However, throughout the stress ranges tested the HCF strength of MA rebar is higher than the TMT rebar. It is noticed in all HCF and LCF experiments in both TMT and MA rebars irrespective of stress/strain ranges the fatigue crack initiates at the root of the transverse ribs. The HCF crack initiates at the root of the transverse ribs that is shown in Fig. 8 for MA rebar. The reason of HCF crack initiation and propagation along the root of transverse rib is elucidated in the finite element simulation section.

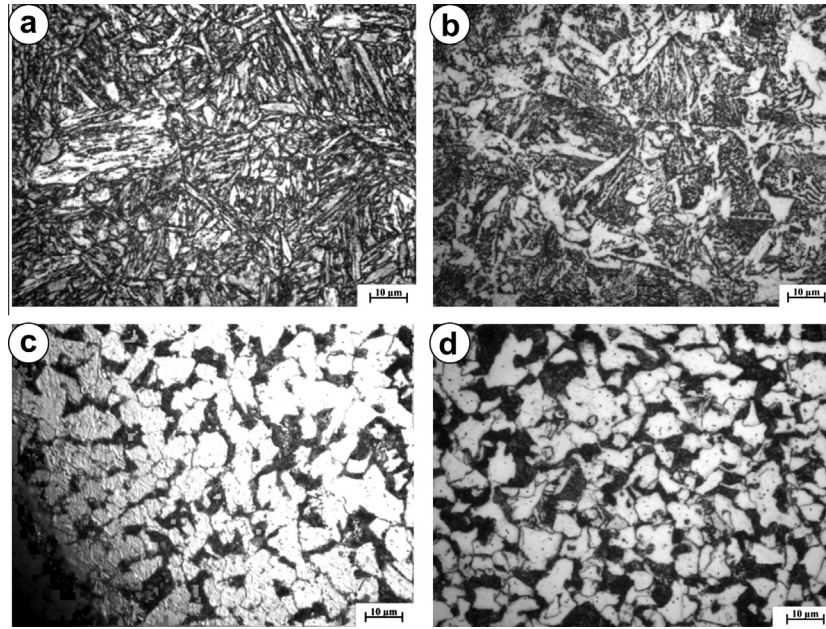


Fig. 4. Optical microstructure of (a) TMT rim region (b) TMT core region (c) MA rim region and (d) MA core region.

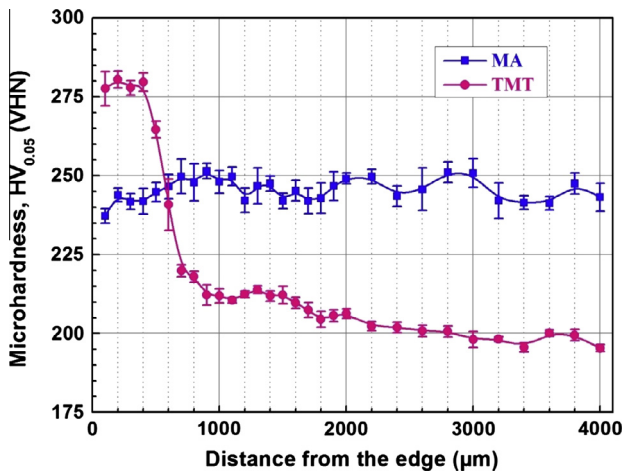


Fig. 5. Vickers micro-hardness of MA and TMT rebars: the distance of profiles are from the edge to center of the rebars.

### 3.4. High cycle fatigue fracture surfaces

The Scanning Electron Microscope (SEM) is used to examine the fracture surface of the tested specimens. Fracture samples of both TMT and MA rebars tested at stress ranges of 328 MPa are selected for SEM examinations. The overall appearances of fracture surfaces are shown in Fig. 9 for TMT rebar and Fig. 10 for MA rebar. It is evident from the micrographs in Figs. 9 and 10 that fatigue cracks in all cases are originated from the surface of the rebars (from the root of the transverse ribs). In addition, each fracture surface exhibits two distinct zones, relatively smooth region corresponds to fatigue crack propagation and final rough region caused by fast/overload fracture. Fast fracture is generally rougher than fatigue fracture surfaces and is more likely to show greater evidence of ridges. On a macroscopic scale the fracture surface is usually normal to the direction of principal tensile stress. The portion from dotted line towards crack origin point represents the fatigue fracture while other side represent fast fracture. The fraction of fatigue

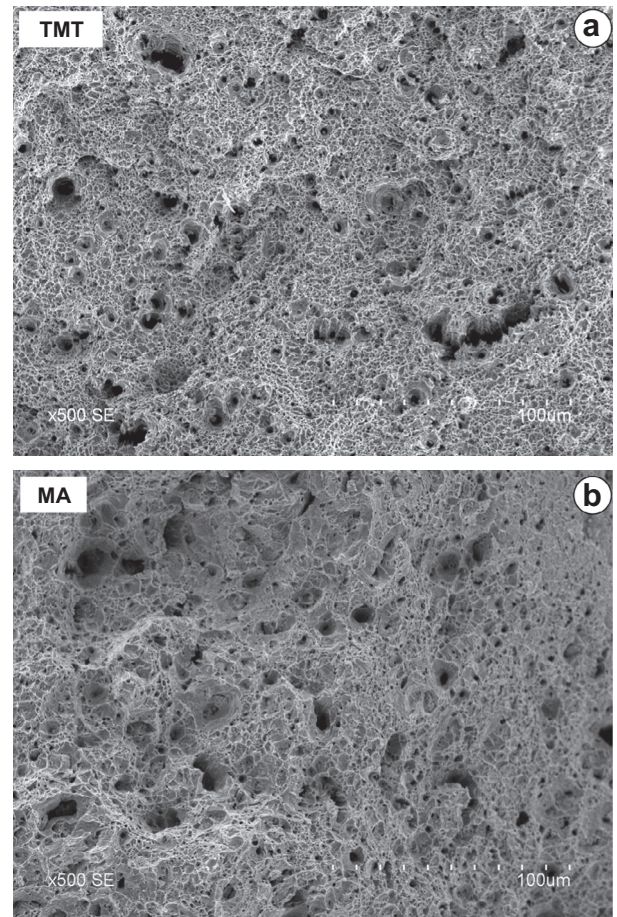


Fig. 6. SEM fractographs of tensile specimens for (a) TMT and (b) MA rebars.

to fast fracture regions depends on the applied stress levels and number of cycles to failure ( $N_f$ ).

Fig. 9d is selected at the middle of fatigue crack initiation and fast fracture that shows enlarged view of fatigue crack propagation

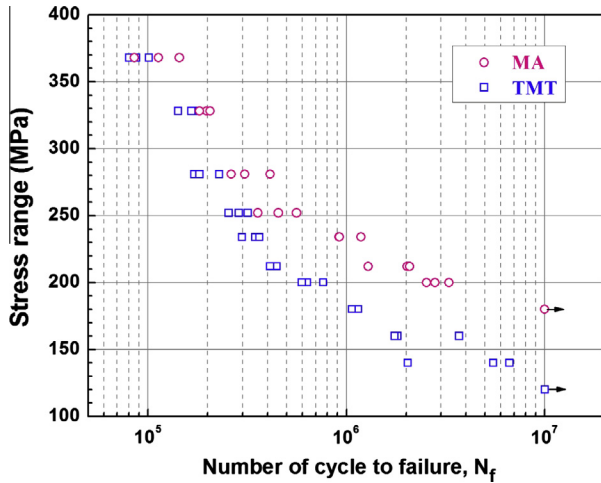


Fig. 7. Stress range versus number of cycle to failure for MA and TMT rebars (R ratio 0.2). The horizontal arrow with data at  $10^7$  cycles indicates without failure.



Fig. 8. HCF crack from transverse rib root.

for TMT rebar. It explains the mechanism of transverse crack propagation in perpendicular direction. The crack propagates until it is made to decelerate by a microstructural barrier such as a grain boundary, inclusions, or hard phase (pearlite or martensite) zones, which cannot accommodate the initial crack growth direction. That is why cracks are not linear rather moves in zigzag fashion. As fatigue crack length increases the local stress and size of plastic deformation zone increases which promotes fatigue crack propagation in a faster manner. At the end when the remaining ligament is unable to bear further load, the sample failed by overload. The ductile overload fracture morphologies characterized by dimples are predominant in the fast/overload fracture surface as shown in Fig. 9c. Similar fracture morphologies are also characterized for MA rebar shown in Fig. 10.

Fig. 11(a) and (b) shows the micro-morphologies are mainly the flat facets and fatigue striations, indicating the fatigue crack growth for TMT and MA rebars tested at  $\Delta\sigma = 328$  MPa. High magnification SEM factography in the fatigue fracture region revealed presence of large number of striations. The most commonly accepted mechanism for the formation of striations on the fatigue fracture surface of ductile metals is the successive blunting and re-sharpening of the crack tip. From SEM micrographs shown in Fig. 11(a) and (b), it can be observed that at high stress intensities, striations arranged in bands can be found marking the crack growth during each load cycle. It can also be observed that in comparison with the TMT rebar, MA rebar exhibits higher striation

density i.e. thickness of one striation is smaller, indicating slower crack propagation per cycle.

### 3.5. Low cycle fatigue performance

Stress amplitude versus number of cycles curve for LCF with different strain amplitudes of TMT and MA rebars are shown in Fig. 12(a) and (b) respectively. Both the rebars display little cyclic hardening (i.e. increase of stress amplitude with number of cycles). Like HCF, fatigue crack also initiate and propagate along the transverse rib root for LCF in both TMT and MA rebars. The cause of fatigue crack initiation and propagation along the transverse rib root is explained in Section 3.6. Comparison between TMT and MA rebar's strain amplitude versus fatigue life is plotted in Fig. 13. Like the HCF life, the LCF lives of MA rebar are also higher in comparison with TMT rebar. With increase of strain amplitude the difference of LCF life between MA and TMT rebar becomes close. UTS/YS ratio (ultimate strength to yield stress ratio) for MA and TMT rebars are 1.4 and 1.18 respectively. Reason for elevated LCF lives of MA rebar is higher uniform elongation and higher UTS/YS ratio in comparison with TMT rebar.

### 3.6. Material model for finite element simulation

The objective of the current study is to understand the effect of transverse rib on stress concentration and cyclic plastic deformation behavior. An elasto-plastic material model is assumed for homogenous and isotropic material. TMT rebar has composite microstructure whereas MA rebar has uniform microstructure. Therefore, the present finite element investigation is conducted on MA rebar. The total strain is decomposed additively into elastic and plastic parts. Small deformation is assumed. For the elastic deformation, the Hooke's law is used. For elastic-plastic deformation, the von Mises yield function ( $F$ ) is employed to describe the initiation of yielding.

$$F = \sqrt{\frac{3}{2}(\bar{S} - \bar{\alpha})(\bar{S} - \bar{\alpha})} - \sigma_0 = 0 \quad (1)$$

where  $\bar{S}$  is the deviatoric stress,  $\bar{\alpha}$  is back stress and  $\sigma_0$  is the cyclic yield stress. In coupled models, plastic modulus calculation is coupled with the kinematic hardening model through a consistency Eq. (2) [20,21], and same consistency equation has been used in this work.

$$dF = \frac{\partial F}{\partial \bar{S}} \cdot d\bar{S} + \frac{\partial F}{\partial \bar{\alpha}} \cdot d\bar{\alpha} = 0 \quad (2)$$

The flow rule has been considered as associative which means that the direction of plastic flow is perpendicular to the yield surface, and described as:

$$d\bar{\varepsilon}^p = d\lambda \frac{\partial F}{\partial \bar{\sigma}} = \frac{3}{2} d\varepsilon_{eq}^p \frac{\bar{S} - \bar{\alpha}}{\sigma_0} \quad (3)$$

$$d\varepsilon_{eq}^p = \sqrt{\frac{2}{3}} d\bar{\varepsilon} \cdot d\bar{\varepsilon} \quad (4)$$

where  $d\bar{\varepsilon}^p$  is the plastic strain increment,  $d\lambda$  is a nonzero operator in associative flow rule,  $d\varepsilon_{eq}^p$  is the equivalent plastic strain increment can be calculated from Eq. (4).

In the current cyclic plasticity model, Chaboche kinematic hardening model [22] is chosen to compute evolution of back stress  $\bar{\alpha}$ . The cyclic yield stress  $\sigma_0$  is kept as constant because cyclic hardening is negligible for MA rebar.

Chaboche kinematic hardening model has excellent predicting capability of low cycle fatigue hysteresis loop [20,21,23,24]. Therefore in the current work, to simulate low cycle fatigue hysteresis

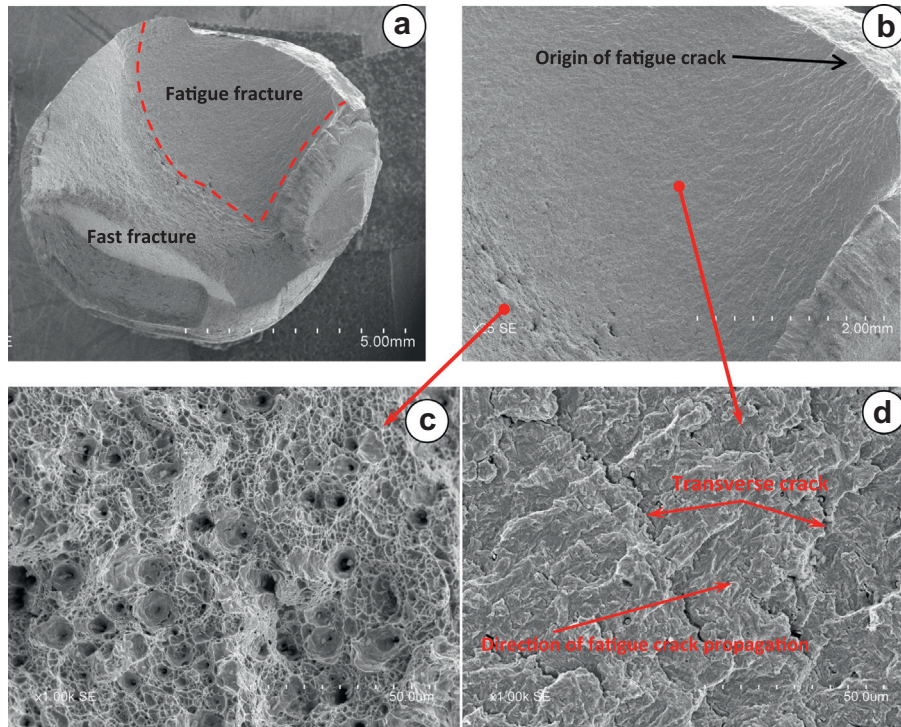


Fig. 9. Fatigue fracture surface of TMT rebar tested at stress range ( $\Delta\sigma$ ) 328 MPa and stress ratio (R) 0.2.

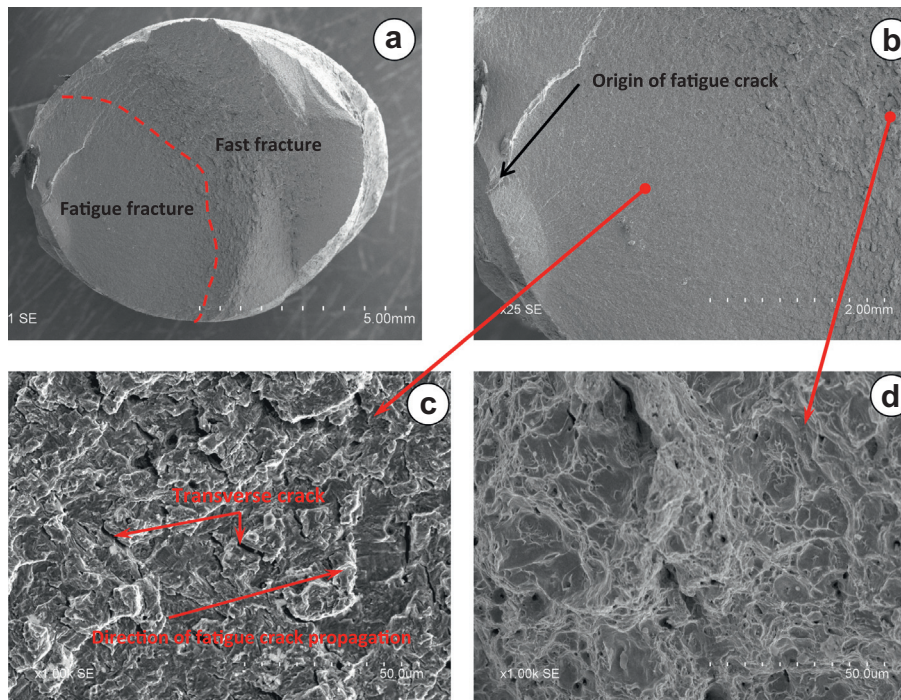


Fig. 10. Fatigue fracture surface of MA rebar tested at stress range ( $\Delta\sigma$ ) 328 MPa and stress ratio (R) 0.2.

loops, Chaboche kinematic hardening model is chosen. Kinematic hardening model proposed by Chaboche [22] is a superposition of three Armstrong and Frederick hardening models. The model can be written in the form

$$d\bar{\alpha} = \sum_{j=1}^3 d\alpha_j$$

$$d\bar{\alpha}_j = \frac{2}{3} C_j d\bar{\epsilon}^p - \gamma_j \bar{\alpha}_j d\bar{\epsilon}_{eq}^p \quad (5)$$

where  $d\alpha$  is the back stress increment,  $d\bar{\epsilon}_{eq}^p$  is the equivalent plastic strain increment,  $C_1, C_2, C_3, \gamma_1, \gamma_2$  and  $\gamma_3$ , are the material constants ( $C_1 > C_2 > C_3$  and  $\gamma_1 > \gamma_2 > \gamma_3 = 0$ ). The details of Chaboche material constants determination procedure is discussed in literatures [20,21,24].

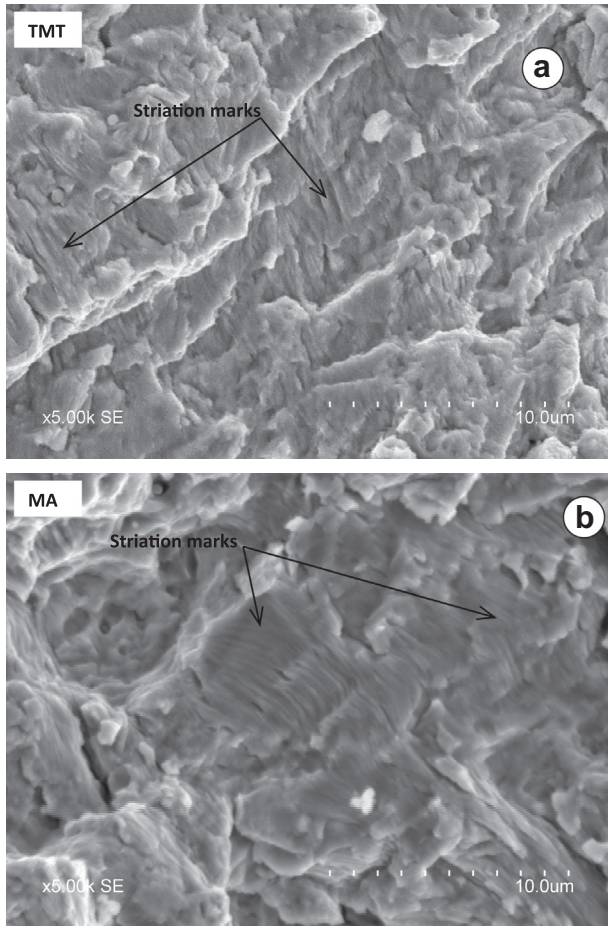


Fig. 11. Fatigue fracture showing formation of striation for (a) TMT and (b) MA rebar tested at  $\Delta\sigma = 328$  MPa.

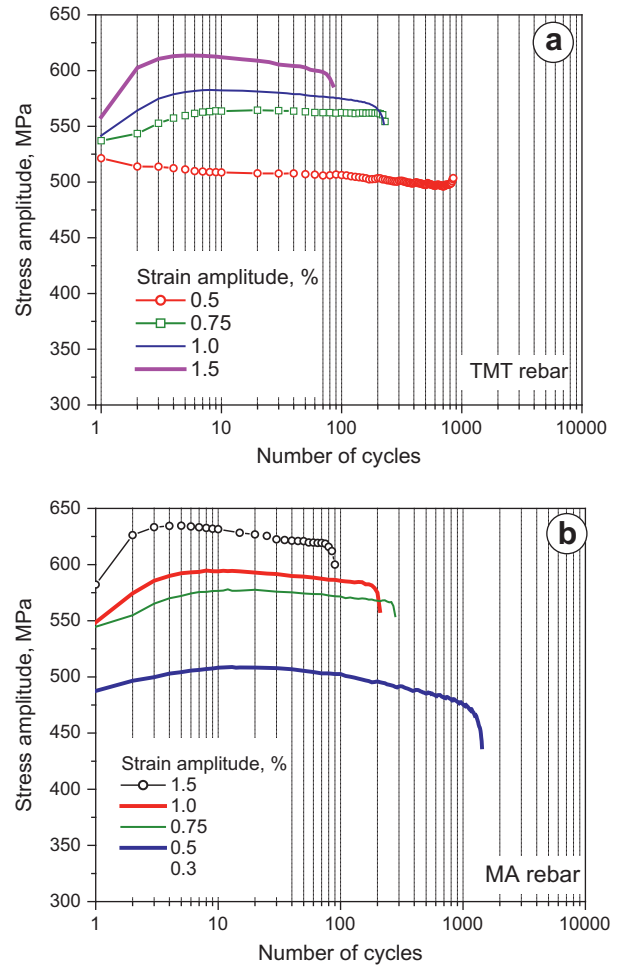


Fig. 12. Stress amplitude versus number of cycles curve for LCF with different strain amplitudes (a) TMT rebar and (b) MA rebar.

Loading part of the stress–strain curve can be represented as:

$$\sum_{j=1}^3 \alpha_j + \sigma_0 = \sigma. \quad (6)$$

The material constants of MA rebar for the cyclic plasticity model are tabulated in Table 2.

Fig. 14 shows the comparison between experimental and simulation hysteresis loop for 1.0% strain amplitude controlled low cycle fatigue. The simulation results matched reasonably well with the experimental results. With this set of material constants, the finite element simulation of MA rebar is conducted and which is discussed in the next section.

3.7. Finite element simulation results for MA rebar

Axi-symmetric geometry (Fig. 15) of the MA rebar is assumed in the present investigation for simplicity which is also adopted by Zheng and Abel [25]. The meshing of the MA rebars axi-symmetric geometry is shown in Fig. 15. Elastic finite element analysis conducted on the same axi-symmetric model with stress amplitude of 300 MPa (below the yield stress). The stress along loading direction (S22) and stress triaxiality is depicted in Fig. 16(a) and (b) during peak tensile loading. Stress concentration at the root of transverse rib is clearly noticed. Zheng and Abel [25] also reported stress concentration due to rib geometry. Due to the presence of transverse rib the cross sectional area perpendicular to the loading direction alters and stress concentration at the root of transverse

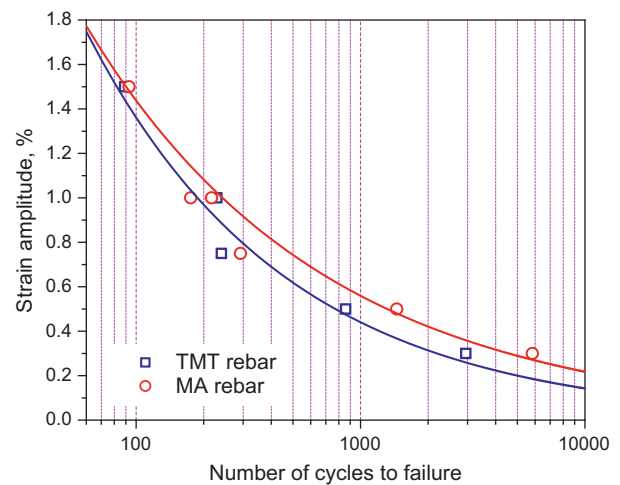
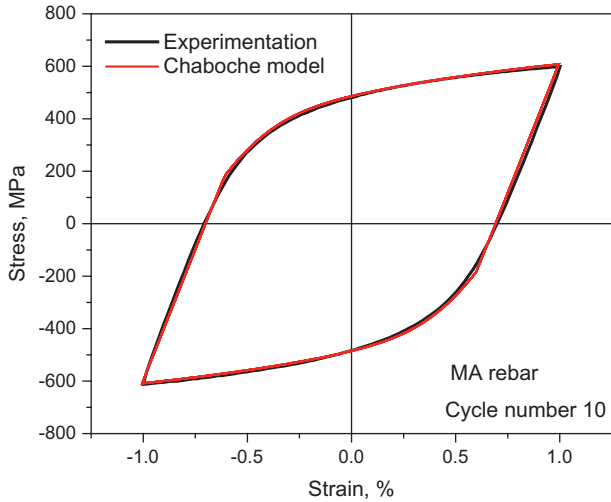


Fig. 13. Comparison between LCF life of TMT and MA rebars.

rib arises for the geometry effect. Stress triaxiality can be defined as the ratio of mean stress and equivalent stress. High stress triaxiality at the root of transverse rib is noticed. Therefore, it can be said from the observation that the stress concentration takes place at the root of transverse rib so HCF crack initiated from

**Table 2**  
Material constants for MA rebar.

$E$ (GPa)	$\nu$	$\sigma_0$ (MPa)	$C_1$ (GPa)	$\gamma_1$	$C_2$ (GPa)	$\gamma_2$	$C_3$ (GPa)	$\gamma_3$	$q_{ps}$ (MPa)	$b$
200	0.3	320	100	750	30	215	2.2	0	90	3.5



**Fig. 14.** Comparison between experimental and simulated hysteresis loop for MA rebar (strain amplitude 1.0%).

the transverse rib root and fatigue crack propagated through the transverse rib root because stress triaxiality is higher in the transverse rib root region.

Elasto–plastic finite element analysis conducted in the same axi-symmetric geometry with Chaboche kinematic hardening model for analysis the cyclic plastic deformation during LCF. Distribution of plastic strain in the loading direction ( $PE_{22}$ ) during first Cycle's tensile peak is shown in Fig. 17. It is clear from Fig. 17 that the plastic deformation localization occurs at the root of transverse rib. Stress triaxiality is computed in each integration point and plotted in Fig. 18. During peak tensile loading, the stress triaxiality at the root of transverse rib is higher. Hence, it can be said from the

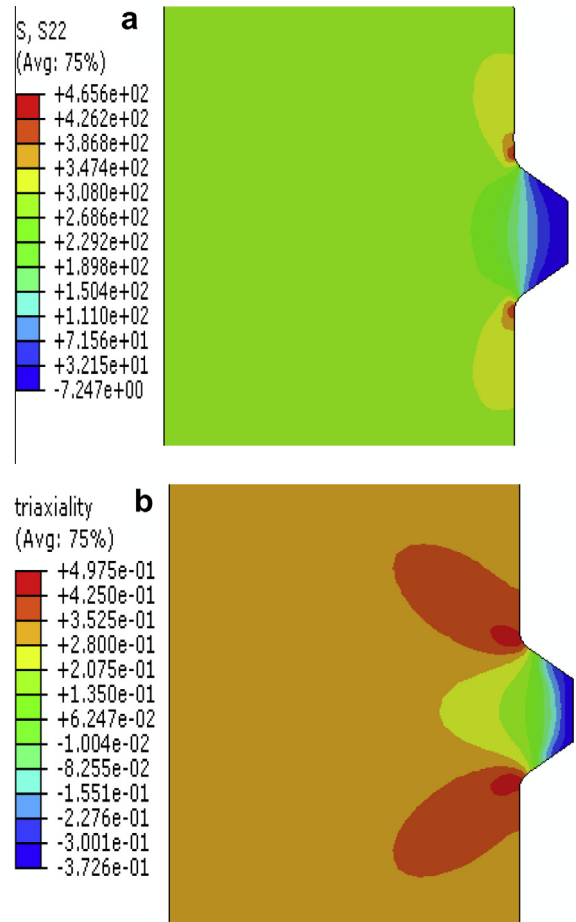


**Fig. 16.** Elastic finite element analysis with stress amplitude of 300 MPa: at peak tensile loading (a) stress along loading direction ( $S_{22}$ ) and (b) stress triaxiality.

investigation that high plastic deformation localization at the root of transverse rib promotes fatigue crack initiation and high stress triaxiality promotes crack growth through this region.

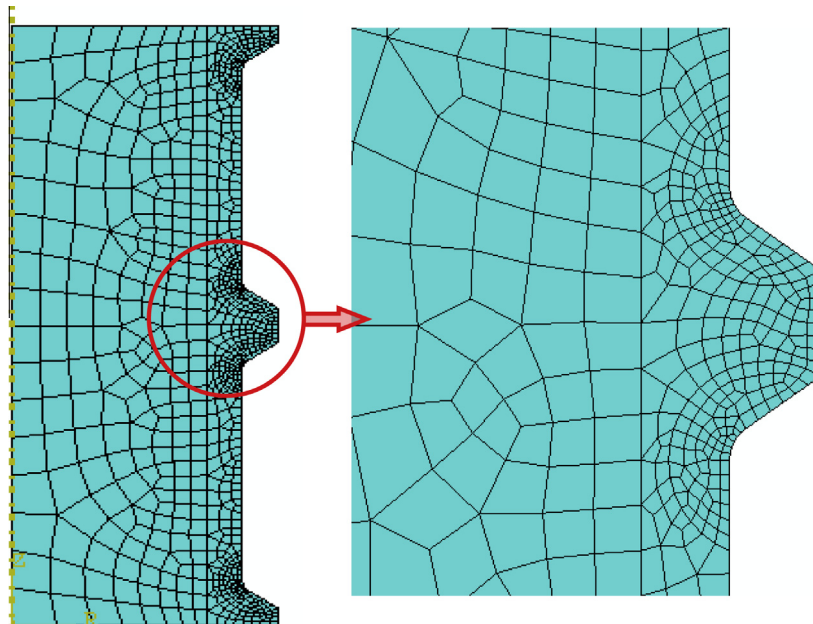


**Fig. 15.** Meshing of axi-symmetric rebar's represented element.

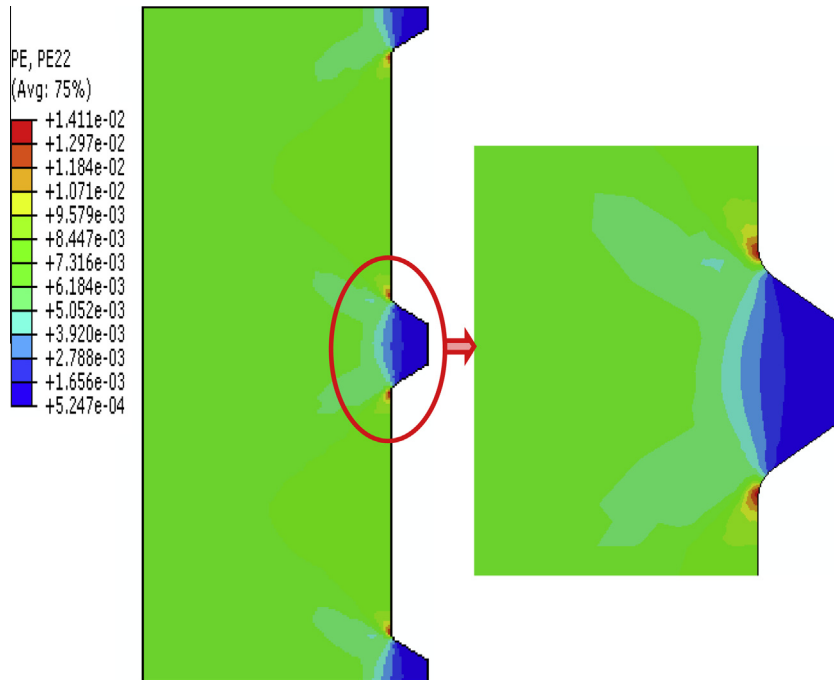


Fig. 17. Distribution of strain in loading direction ( $PE_{22}$ ) during first cycle's tensile peak: deformation concentrated at the root of transverse rib.

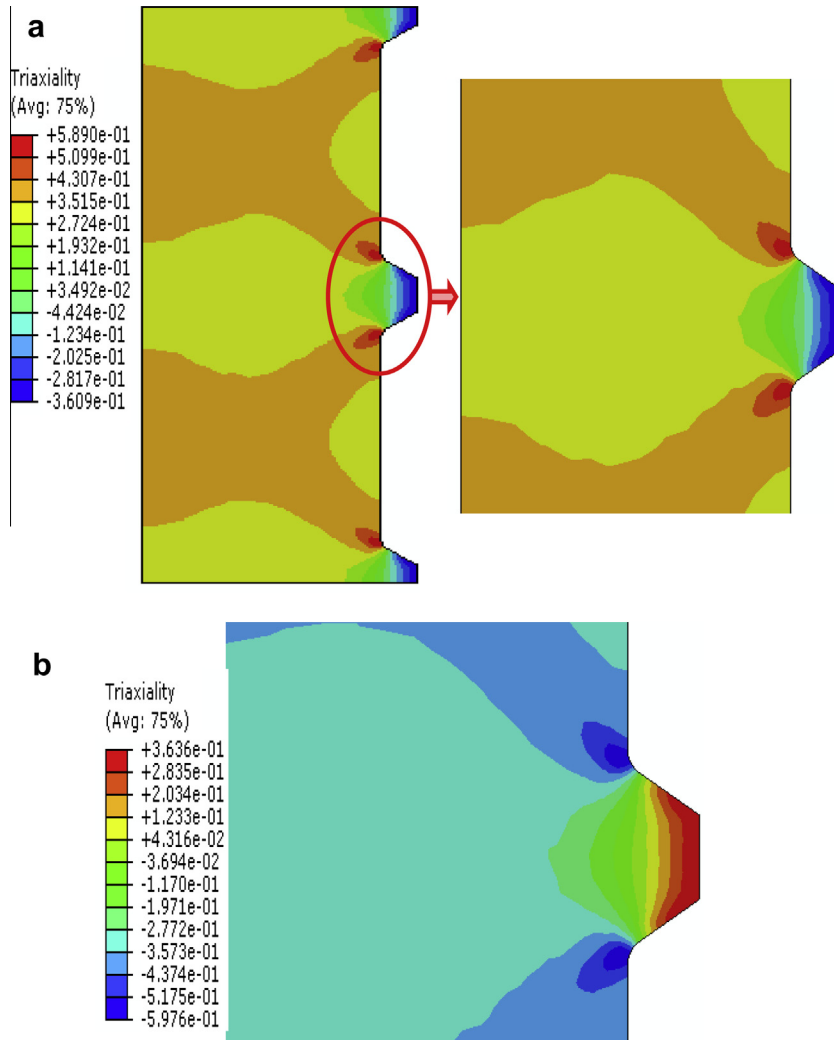
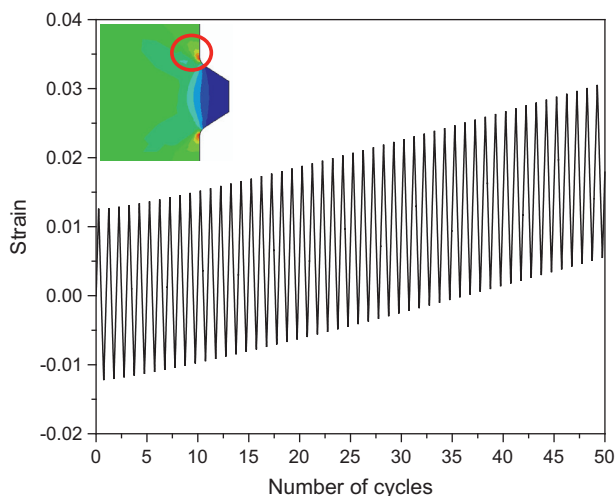


Fig. 18. Distribution of stress triaxiality during (a) first cycle's tensile peak: high stress triaxiality at the root of transverse rib and (b) first cycle's compressive peak.



**Fig. 19.** Response of strain in loading direction ( $LE_{22}$ ) with number of cycles at the root of transverse rib: positive strain accumulation at the root of transverse rib.

At the root of transverse rib, the response of strain in loading direction with number of cycles is shown in Fig. 19. There is clear evidence that positive strain accumulation is taking place at the root of transverse rib. This positive strain accumulation can intensify the fatigue damage [26–28]. Therefore, the fatigue crack initiates from the transverse rib root which is influenced by the deformation concentration as well as the positive strain accumulation. Of course, local surface flaw or material defects have an influence on fatigue damage. In absence of flaws or defects, fatigue crack should initiate from the root of transverse rib only. The same observation (fatigue crack always initiates from the root of transverse rib) is noticed in experimental results.

#### 4. Conclusions

In this current work, HCF and LCF behavior of MA and TMT rebar at room temperature are presented. Diameter and rib profiles of MA and TMT rebars are exactly same. MA rebar exhibits better HCF and LCF performances than TMT rebar. Elevated LCF lives of MA rebar can be explained by superior uniform elongation and higher UTS/YS ratio in MA rebar in comparison with the TMT rebar. HCF factography reveals that higher striation density in MA rebar in comparison with TMT rebar which indicates slower crack propagation per cycle in MA rebar. Fatigue crack initiates from the transverse rib root and propagate along the same region in all HCF and LCF experiments for both kinds of rebar.

Elastic finite element simulation (represents HCF) result reveals that stress concentration and high stress triaxiality developed occurs at the root of the transverse rib. Elasto-plastic finite element simulation (represents LCF) result reveals that plastic strain localization occurs at the root of the transverse rib and also tensile strain accumulation takes place at the same region. High stress triaxiality is also detected during elasto-plastic finite element simulation at the root of the transverse rib which facilitates the fatigue crack propagation along the transverse rib root.

#### References

- [1] Khudik YT, Ivchenko AV, Chaikovskii OA, Madtjan SA, Kostyuchenko MI, Surikov IN. Thermo-mechanically strengthened 25G2S reinforcing steel of strength class At-IVS. *Steel USSR* 1988;18(6):272–7.
- [2] Frommann K, Vlad CM. Mechanical and Technological Properties of TEMPRIMAR Weldable High Strength Rebars. In: 27th Mechanical working and steel processing conf. proc., vol. 23. Iron and Steel Society; 1986, p. 901–07.
- [3] Madatyan SA. Main trends in development of production and use of steel reinforcing bars. *Steel USSR* 1991;21(7):322–5.
- [4] Kundu S, Mukhopadhyay A, Chatterjee S, Chandra S. Modelling of microstructure and heat transfer during controlled cooling of low carbon wire rod. *ISIJ Int* 2004;44(7):1217–23.
- [5] Sheng GM, Gong SH. Investigation of low cycle fatigue behavior of building structural steels under earthquake loading. *Acta Metallurg Sin (English Letters)* 1997;10(1):51–5.
- [6] Mander JB, Panthake FD, Kasalanati A. Low-cycle behavior of reinforcing steel. *J. Mater. Civ. Eng.* 1994;6(4):453–68.
- [7] Apostolopoulos CA, Papadopoulos MP. Tensile and low cycle fatigue behavior of corroded reinforcing steel bars S400. *Constr Build Mater* 2007;21:855–64.
- [8] Apostolopoulos CA. Mechanical behavior of corroded reinforcing steel bars S500s tempore under low cycle fatigue. *Constr Build Mater* 2007;21(7):1447–56.
- [9] Bar HN, Sivaprasad S, Narasaiah N, Paul SK, Sen BN, Chandra S. Low cycle and ratcheting fatigue behavior of high UTS/YS ratio reinforcing steel bars. *J Mater Eng Perform* 2013;22(6):1701–7.
- [10] Abdalla JA, Hawileh RA, Oudah F, Abdelrahman K. Energy – based prediction of low-cycle fatigue life of BS 460B and BS B500B steel bars. *Mater Des* 2009;30:4405–13.
- [11] Hawileh RA, Abdalla JA, Oudah F, Abdelrahman K. Low-cycle fatigue life behaviour of BS 460B and BS B500B steel reinforcing bars. *Fatigue Fract Eng Mater Struct* 2010;33(7):397–407.
- [12] Shi Y, Wang M, Wang Y. Experimental and constitutive model study of structural steel under cyclic loading. *J Constr Steel Res* 2011;67:1185–97.
- [13] Shi G, Wang M, Bai Y, Wang F, Shi Y, Wang Y. Experimental and modeling study of high-strength structural steel under cyclic loading. *Eng Struct* 2012;37:1–13.
- [14] *Steel Concrete and Composite Bridges, BS 5400*. London: British Standards Institution; 1978.
- [15] Tilly GP. Fatigue of steel reinforcement bars in concrete: a review. *Fatigue Eng. Mater. Struct.* 1979;2:251–68.
- [16] Apostolopoulos C, Passialis V. Use of quality indices in comparison of corroded technical steel bars B500c and S500s on their mechanical performance basis. *Constr Build Mater* 2008;22(12):2325–34.
- [17] BS 4449: Steels for the reinforcement of the concrete – weldable reinforcing steels – bars, coil and decoiled product specification; 2005.
- [18] ASTM designation E 606-92. Standard practice for strain-controlled fatigue testing.
- [19] Apostolopoulos C, Matikas T, Kodjaspirov G, Diamantogiannis G, Apostolopoulos A. The role of MnS inclusion in structural integrity of steel bar under seismic loads. In: Proc of the 10th international conference on advanced metal materials and technologies (AMMT'13). Saint Petersburg, Russia; 25–29 June 2013, p. 495–01.
- [20] Bari S, Hassan T. Anatomy of coupled constitutive models for ratcheting simulations. *Int J Plasticity* 2000;16:381–409.
- [21] Paul SK, Sivaprasad S, Dhar S, Tarafder M, Tarafder S. Simulation of cyclic plastic deformation response in SA333 C-Mn steel by a kinematic hardening model. *Comput Mater Sci* 2010;48(3):662–71.
- [22] Chaboche JL. On some modifications of kinematic hardening to improve the description of ratcheting effects. *Int J Plast* 1991;7:661–78.
- [23] Rezaiee-Pajand M, Sinaie S. On the calibration of the Chaboche hardening model and a modified hardening rule for uniaxial ratcheting prediction. *Int J Solids Struct* 2009;46(16):3009–17.
- [24] Paul SK, Tarafder S. Cyclic plastic deformation response at fatigue crack tips. *Int J Press Vessels Pip* 2013;101:81–90.
- [25] Zheng H, Abel A. Stress concentration and fatigue of profiled reinforcing steels. *Int J Fatigue* 1998;20(10):767–73.
- [26] Paul SK, Sivaprasad S, Dhar S, Tarafder S. Key issues in cyclic plastic deformation: experimentation. *Mech Mater* 2011;43(11):705–20.
- [27] Lin YC, Chen XM, Chen G. Uniaxial ratcheting and low-cycle fatigue failure behaviors of AZ91D magnesium alloy under cyclic tension deformation. *J Alloy Compd* 2011;509(24):6838–43.
- [28] Lin YC, Liu ZH, Chen XM, Chen J. Uniaxial ratcheting and fatigue failure behaviors of hot-rolled AZ31B magnesium alloy under asymmetrical cyclic stress-controlled loadings. *Mater Sci Eng, A* 2013;573:234–44.